JOURNAL OF AIRCRAFT
Vol. 39, No. 6, November–December 2002

Drag Prediction of Engine–Airframe Interference Effects Using Unstructured Navier–Stokes Calculations

O. Brodersen*
DLR, German Aerospace Research Center, 38108 Brunswick, Germany

Navier–Stokes calculations on hybrid grids using the TAU software of the MEGAFLOW project are performed to compute engine installation drag for the DLR, German Aerospace Research Center, F6 transport aircraft configuration at cruise flight conditions with conventional and with very-high-bypass-ratio nacelles at three and two different locations, respectively. The results are verified by a comparison with experimental data from different wind-tunnel campaigns carried out with Office National d'Etudes et de Recherches Aerospatiales. Numerical discretization errors are reduced by several steps of grid adaptation, resulting in grid densities up to 8.4×10^6 nodes. It is demonstrated that the installation drag of the different configurations, which vary only a few drag counts (10^{-4}), can be computed consistently, although the total drag forces are predicted lower than results of experiments. Successive grid refinement leads to a decrease of the differences between calculated and measured installation drag.

Nomenclature

C_D	=	total drag coefficient
C_L	=	total lift coefficient
c	=	local chord length
c_p	=	pressure coefficient
M	=	Mach number
N	=	number of grid points
Re	=	Reynolds number
s	=	half span
x	=	horizontal engine position
y^+	=	normal distance from a solid wall, when normalized ($y \cdot u_\tau \cdot \rho/\mu_{\text{laminar}}$)
z	=	vertical engine position
α	=	angle of incidence
η	=	half-span coordinate, dimensionless
Λ	=	wing aspect ratio
λ	=	wing taper
ρ	=	density
Φ_{LE}	=	wing leading-edge sweep angle

Subscripts

D-install	=	installation drag
D-with-engine	=	total drag of the configuration with nacelles
D-clean	=	total drag of the wing–fuselage configuration
D-internal	=	internal drag of the through-flow nacelle
TE	=	trailing edge

Introduction

ONE key aspect during the design of an enhanced civil transport aircraft is the efficient integration of engines on a wing in high- and low-speed configurations.[1,2] The tendency to increase the bypass ratio of turbofan engines from approximately 6 up to 10 during the last decade, which was mainly driven by the objective to reduce the specific fuel consumption and engine jet noise, can result in a lift loss and an increasing installation drag. This is directly related to the engine size and location, as has been demonstrated in several European projects, for example, Ducted Propfan Investigations, Engine Integration on Future Aircraft, Aircraft Drag and Thrust Analysis (AIRDATA).[3–8] Although aerodynamic effects are not the only important factors during engine integration,[1] the work presented here is focused on numerical and aerodynamic questions.

Since 1990, successive investigations in the field of engine–airframe integration have been performed by different researchers.[9–16] At the German Aerospace Research Center, DLR, the F6 [high-speed with through-flow nacelles (Fig. 1)] and ALVAST (low- and high-speed with turbopowered simulators) configurations, which are similar to an Airbus-type aircraft, have been extensively used for analysis. The work on the F6 included wind-tunnel campaigns in cooperation with Office National d'Etudes et de Recherches Aerospatiales (ONERA) and numerical computations using Euler and Navier–Stokes techniques for different engine types and positions.[9,16–20]

Although in the early 1990s the first steps toward unstructured computational fluid dynamics (CFD) techniques were undertaken at DLR, numerical investigations have been concentrated on the multiblock structured grid approach for the few last years for reasons of numerical accuracy. It had been demonstrated that Euler and simplified Navier–Stokes solutions can be used to predict and understand the main interference effects and flow features, for example, lift loss, shock movement, and flow acceleration. However, the advantages of numerical studies such as the decomposition of lift and drag for the aircraft components could not be fully utilized because Navier–Stokes results with high accuracy and verified by grid refinement studies could only be obtained with very great effort. In particular the prediction of the installation drag

$$C_{D\text{-install}} = C_{D\text{-with-engine}} - C_{D\text{-clean}} - C_{D\text{-internal}}$$

for different engines and their positions was too time consuming to apply in an industrylike project environment.

Although Navier–Stokes results for realistic aircraft configurations have been available for several years, the importance of CFD validation and verification has been stressed by the CFD community only recently (Refs. 21–24 and presentation at Daimler–Chrysler, Stuttgart, Germany, 10 June 1998 by P. Rubbert, "On Replacing the Concept of CFD Validation with Uncertainty Management"). In the framework of the national German project MEGAFLOW I, an extensive validation and verification process was started a few years ago for structured and unstructured Navier–Stokes software using different configurations.[25] In addition to extensive tests at DLR and in industry, verification studies at DLR for the F6 configuration have been performed applying structured grid refinement, different turbulence models, and numerical parameter variations. It was demonstrated that even with 16×10^6 structured grid points

Received 1 March 2002; revision received 28 May 2002; presented as Paper 2002-2414 at the 19th Applied Aerodynamics Conference, Anaheim, CA, 11–14 June 2002; accepted for publication 29 June 2002.

*Research Scientist, Institute of Aerodynamics and Flow Technology.

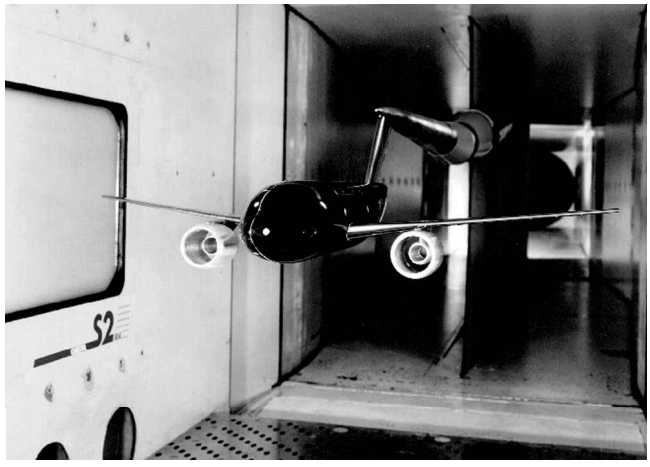

Fig. 1 DLR-F6 model with VHBR nacelles in the ONERA S2MA wind tunnel.

for a wing–fuselage configuration a change of the drag coefficient of nearly 2.5% compared to a zero mesh element size extrapolated value can be observed, depending on the grid and flow conditions.[26]

The structured grid generation for this type of configuration was a time-consuming and labor-intensive process. Between one and three months were needed for the generation of suitable structured grids for aircraft configurations at cruise and high-lift conditions. It was found that structured grids for different engines and their positions, especially when closed coupled, could not be realized in a timeframe demanded by industry. For these reasons and because for configurations with deployed high-lift devices grid generation becomes even more complex, it was decided to strengthen the unstructured/hybrid activities in the MEGAFLOW project. Although the potential of unstructured techniques has been already demonstrated by several other researchers,[27–29] the author still sees the necessity to verify the installation drag prediction capabilities of a hybrid Navier–Stokes system. This holds true also for the TAU software[30–33] in combination with hybrid grid-generation techniques proposed by Kallinderis[34] and Khawaja and Kallinderis,[35] which are integrated in the commercial highly automated software system Centaur™ developed by CentaurSoft.

Although in the past the DLR engine/airframe research activities have been focused on understanding basic flow features of these configurations, the objective now is to compute the installation drag for conventional and very-high-bypass-ratio (VHBR) nacelles for different geometric positions precisely. This becomes important for future applications of numerical optimization techniques that take into account the engine position, nacelle, and wing shape simultaneously. Without a reproducible accuracy, design modifications may lead to nonoptimal solutions. Thus, results have to be verified using grid refinement techniques and have to be compared to experiments to determine whether the installation drag for different configurations observed in the wind tunnel can be predicted within a reasonable accuracy.

The investigations presented here will concentrate on installation effects at cruise conditions using a large set of experimental data from different projects. Studies of installation effects with powered engines and high-lift systems will be performed in other projects, for example European High-Lift Program and AIRDATA.[6–8,36]

Aircraft Configuration

The DLR-F6 wind-tunnel model represents a twin-engine wide-body aircraft of Airbus type and is derived from the ealier DLR-F4 configuration.[37] For a design cruise Mach number of $M_\infty = 0.75$, the lift coefficient is $C_L = 0.5$. Figure 2 shows the geometrical data. The aspect ratio is $\Lambda = 9.5$, the leading-edge angle is $\Phi_{LE} = 27.1$ deg, and the taper ratio is $\lambda = 0.3$.

The engines are represented by through-flow nacelles. Three different nacelles are available, two CFM-56-like types with a long duct and a short duct and a VHBR nacelle. All nacelles have an

Table 1 Nacelle positions

Nacelle	x_{TE}/c	z_{TE}/c
CFM-56-long, position 1	0.49	−0.189
CFM-56-long, position 2	0.30	−0.189
CFM-56-long, position 2	0.30	−0.250
CFM-56-short, position 1	0.04	−0.160
VHBR, position 1	−0.05	−0.120
VHBR, position 2	0.00	−0.120

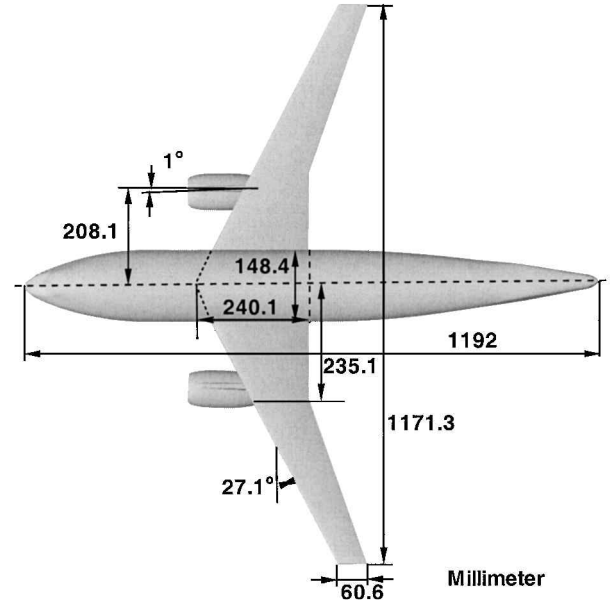

Fig. 2 Planform of the DLR-F6 model with through-flow nacelles.

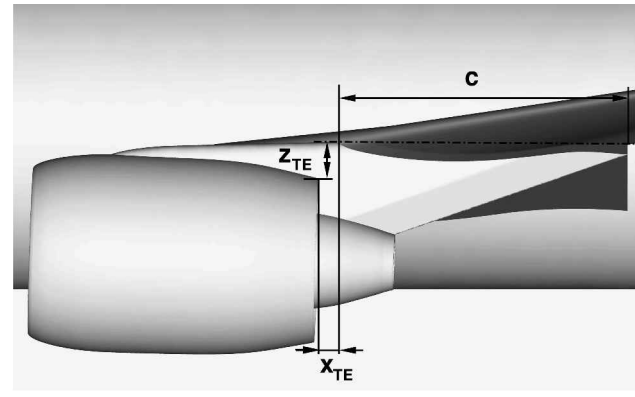

Fig. 3 Definition of a nacelle position.

axi-symmetrical shape. The mass flow represents the real engine intake mass flow. The engine exit flow is not reproduced exactly. In spite of this shortcoming, in the experiments as well as in the numerical investigations verification is not affected negatively. For the conventional long nacelle three positions, for the conventional short nacelle one position, and for the VHBR nacelle two different positions have been analyzed in the wind tunnel and in these computations. The positions are characterized by a distance in horizontal x and vertical z direction between the wing leading edge and the nacelle upper trailing edge, x_{TE} and z_{TE}, in relation to the local wing chord length c, respectively (Fig.3 and Table 1).

Experiments

For the different configurations, test campaigns have been performed from 1990 to 1998 in the ONERA S2MA pressurized wind tunnel (Fig. 1). The F6 model was sting mounted in the 1.77×1.75 m transonic test section. Pressure distributions are measured by 288 pressure taps located in 8 spanwise wing sections and

47 locations in 3 radial sections of the nacelle. The investigations presented here will use sections at 23.8, 33.1 (inboard of pylon), and 37.7% (outboard of pylon) half-span positions to analyze c_p. The Mach number was varied between $M_\infty = 0.6$ and 0.8, and the Reynolds number was kept constant at $Re = 3 \times 10^6$. During a single campaign, standard deviations of drag coefficients between 0.3 and 0.9 drag counts (1 drag count $= 10^{-4}$) have been measured. In each test campaign wing–fuselage measurements have been included for reference purposes. It has been observed that drag increased slightly from one campaign to another over the eight-year period, probably due to a small deterioration of the geometry. The results presented in this work include the variations of the experimental data.

Flow Solution Method

Hybrid Unstructured Flow Solver TAU

For the solution of the Reynolds averaged Navier–Stokes equations, the DLR TAU software[30–33] is used, which is still under development. TAU is a finite volume vertex-based solver with an edge-based data structure. Together with a dual-grid technique, the use of different element types, for example, tetrahedrals, prismatic cells, pyramids, and hexahedrals, is possible. The discretization of the convective fluxes has been realized with a second-order central difference scheme with scalar dissipation, which will be used for these investigations. Roe- and Advection Upwind Splitting Method-type upwind schemes are also implemented. The viscous fluxes are discretized using central differences. Time integration to steady state is accomplished with a three-stage Runge–Kutta scheme. For convergence acceleration local time stepping, residual smoothing, multigrid, and message passing interface-based parallelization is available and used here. One- and two-equation turbulence models are implemented. The Spalart–Allmaras model[38] with Edwards modification is applied in these investigations.

Hybrid Grid Generation

It is well known that the density and quality of grids is of great importance for solution accuracy. Therefore, it is necessary to have a grid-generation system that is on the one hand able to generate high-quality hybrid grids and on the other hand able to perform this as automatically as possible. DLR uses the software package Centaur from CentaurSoft. The system consists mainly of two parts. First, an interactive program an initial graphics exchange specification reads in CAD data in IGES format and performs some CAD cleaning if necessary. It also allows the modification of boundary conditions and element sizes if the user does not prefer the default values. Different parameters control the surface and prismatic and tetrahedral element sizes. A selection of user-definable sources offers the possibility to generate grids of the desired density in certain areas. In a second step, the complete grid will be computed automatically. The wing surfaces are meshed with triangles that have been stretched in spanwise direction by a factor of approximately 2.5 to reduce the number of cells in the spanwise direction, where only small gradients of the flow are expected. In the flow direction, the wing is resolved at the root section by approximately 500 points for the upper and lower surface together. Normal to all surfaces, 24 prismatic cells with an intial stretching ratio of approximately 1.22 are generated. Figures 4 and 5 show grid cells in the symmetry plane and for a fieldcut through the VHBR nacelle. Particular attention was given to obtain a smooth transition of sizes between the prismatic and tetrahedral elements.

In regions of CAD panel intersections or in close proximity, the number of prismatic cells can be reduced automatically if desired to maintain grid quality. Here layer reductions have been nearly avoided completely so that in the junctions of wing–fuselage, wing–pylon, or pylon–nacelle the minimum number of prismatic layers is 18. The regions up to the far field are represented by tetrahedral elements. In areas where the number of prismatic layers has been reduced, pyramids can become necessary to connect faces of prismatic cells and tetrahedral elements.

The initial grid densities are close to 2.6×10^6 nodes for the wing–fuselage and approximately 4.6×10^6 nodes for the configurations

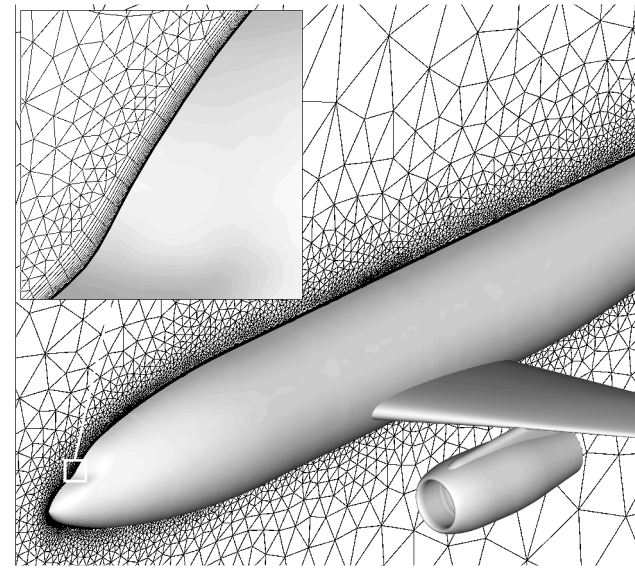

Fig. 4 Hybrid grid in the symmetry plane for the DLR-F6 model, conventional long nacelle, position 1.

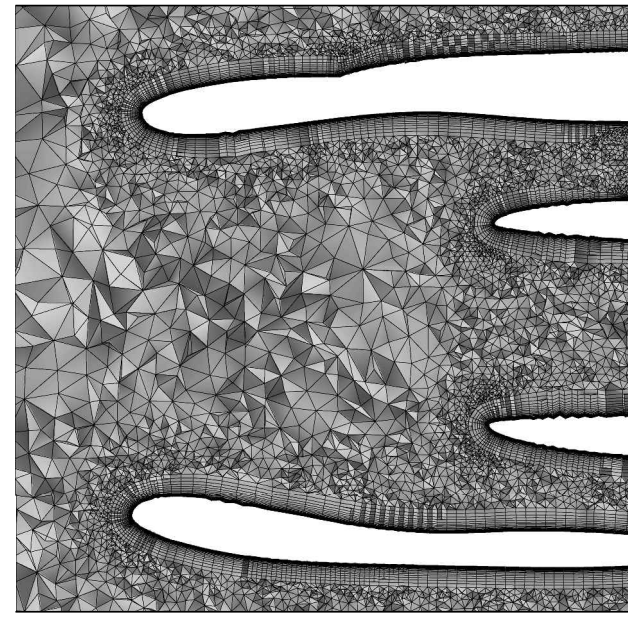

Fig. 5 Fieldcut through the initial hybrid grid, VHBR nacelle.

with nacelles. These grids can be generated in one to two days including the setup when the accuracy of the CAD geometry fulfills the requirements for a solid model. Figure 6 presents a fieldcut through the wing and the CFM-56-long nacelle and displays the grid density of the inital grid in the wake region controlled by a user-specified source.

Grid Adaptation

Solution-based grid adaptation is used to refine elements. A combination of the Centaur and TAU adaption[32] is applied using velocity and total pressure gradients because Centaur takes the original CAD data for the projection of new surface nodes into account, whereas TAU shows better adaptation results in the flowfield and in the boundary layer. The target $y^+ = 0.9 \pm 0.3$ was reached for the complete configuration for all cases.

Three adaptations have been performed for the wing–fuselage and for the CFM-56-long nacelle configurations. Two adapations for the CFM-56-short and for the VHBR configurations had been necessary to obtain comparable grids and to avoid grid sizes exceeding 9×10^6 nodes to limit computational costs. The grid densities for the various configurations are listed in Table 2.

Table 2 Grid densities (10^6 nodes)

Configuration, grid level	Wing–fuselage	CFM-long 1	CFM-long 2	CFM-long 3	CFM-short	VHBR 1	VHBR 2
Initial	2.58	3.79	3.97	3.73	4.03	4.70	4.55
Final grid	5.52	7.46	7.44	7.74	8.72	8.46	8.19

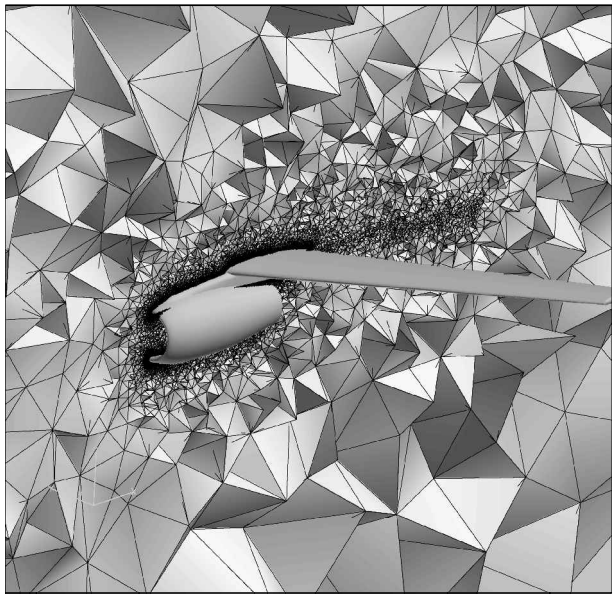

Fig. 6 Fieldcut through the initial hybrid grid, conventional long nacelle, position 1.

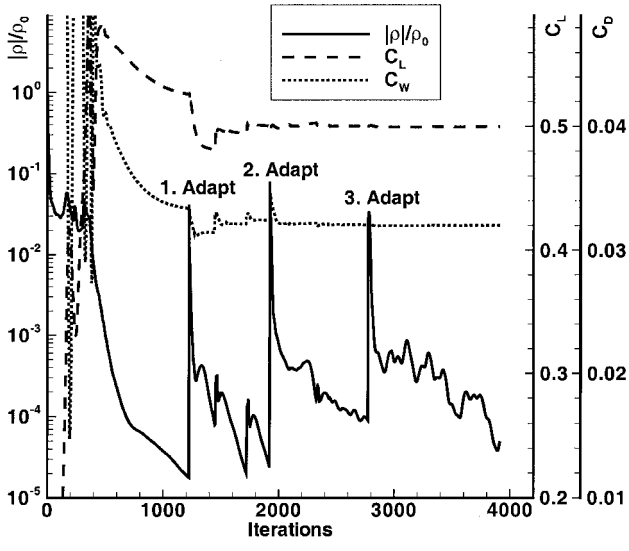

Fig. 7 Convergence history for the DLR-F6 with conventional long nacelle, position 1.

Numerical Results

Calculations have been performed for a Mach number $M_\infty = 0.75$ for a range of lift coefficients $C_L = 0.2, 0.3, 0.4$, and 0.5 using a fixed transition at the same position as for the wind-tunnel model. After approximately 1200 multigrid iterations on an initial grid, the main flow features are established, and the first grid adaptation has been started. Then the incidence was modified to obtain a specified target lift. Before a next adaptation was performed, the target lift had to be reached so that C_L is within a tolerance of 0.0001 and C_D does not vary more than 0.000025 or 0.25 drag counts. Figure 7 shows a typical convergence rate of density residuals, lift, and drag. The

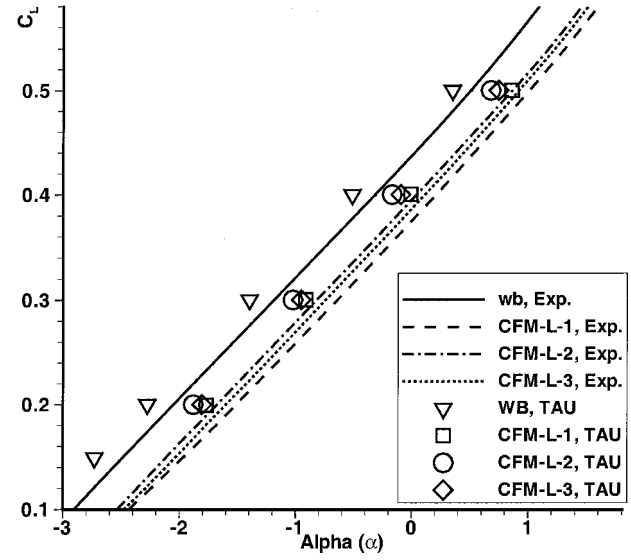

Fig. 8 Lift coefficients for DLR-F6 with conventional long nacelles.

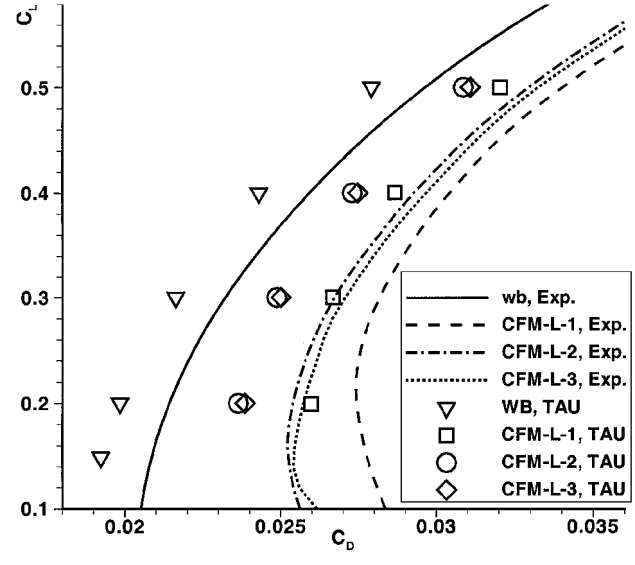

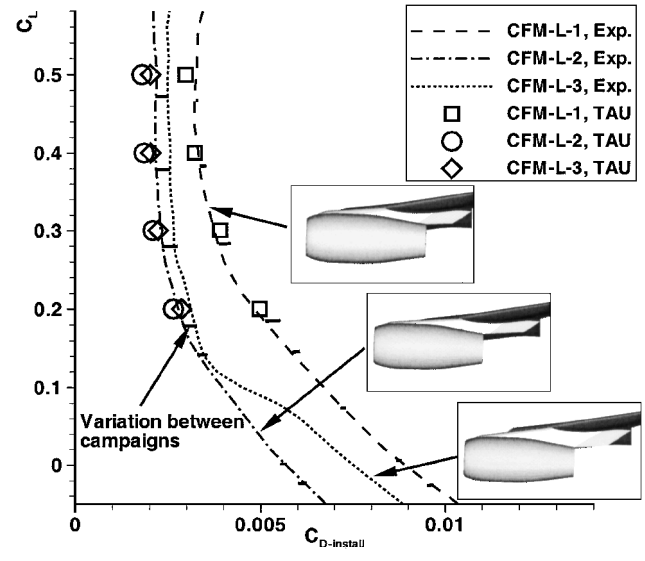

Fig. 9 Drag coefficients and installation drag for the DLR-F6 with conventional long nacelles.

main peaks appear due to a restart with an adapted grid, wheras the small disturbances are results of angle modifications to meet the target lift. It was of great importance that the complete parameter setting for the grid generation, the TAU input, and the adaptation be kept constant for all configurations.

When four processors on a NEC-SX5 vector computer were used, the computational turnaround time, including three grid adaptations with node numbers up to 7.7×10^6 for the conventional long nacelles, averaged to approximately 60 h CPU time to finish a computation for one configuration.

CFM-56 Nacelles

Polars

For verification purposes, the comparison of numerical results with experimental data, as well as grid refinement studies, are of interest. Figure 8 shows the comparison of the computed lift polar (finest grid) for different CFM-56-long nacelle positions and the wing–fuselage configuration together with the experimental data. The differences of C_L vs α for the nacelle positions can be computed. A nearly constant angle shift between the experiments and the numerical results is observable. The drag polars for the four configurations are shown in Fig. 9. The results for the finest grid are compared with experiments. The standard deviation of the experiments during one campaign is approximately equivalent to the thickness of the curves, and the increase of drag over the years from one wind-tunnel campaign to another is given by horizontal lines at several lift coefficients. The experiments show a variation of less than 1 drag count during a test but up to 7 drag counts between different campaigns. The differences between the configurations due to the varying nacelle positions are not significanlty affected by this effect. It can be determined that the nacelle position 2 shows the minimal total and installation drag for the computations, as well as in the experiments.

Although an offset between the calculations and the wind-tunnel data of approximately 16 drag counts is visible for all configurations, the small differences due to varying engine positions can be computed within an accuracy of less than 2 drag counts for the selected lift coefficients. Based on these results and the value for $C_{D\text{-internal}}$, which was measured in calibrations tests (for CFM-56-long, $C_{D\text{-internal,experiment}} = 11.6$ drag counts) and computed ($C_{D\text{-internal,numeric}} = 11.5$ drag counts), the installation drag can be evaluated. Figure 9 shows the installation drag $C_{D\text{-install}}$ for the conventional long nacelle. Its increase for lower lift coefficients is calculable. The too low drag values seen in Fig. 9 have been compensated partially so that the offset to the experimental data could be reduced to 1–4 drag counts and the differences of installation drag can be computed (Table 3). The deviations are approximately the same as observed for different wind-tunnel test campaigns.

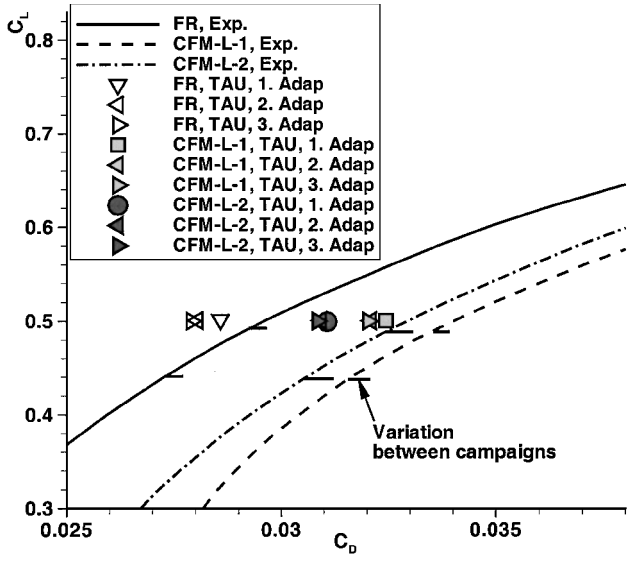

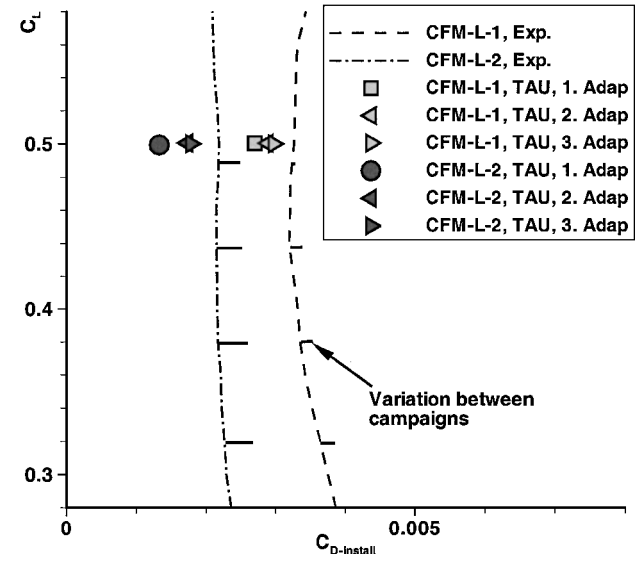

Fig. 10 Influence of grid density overall and on installation drag.

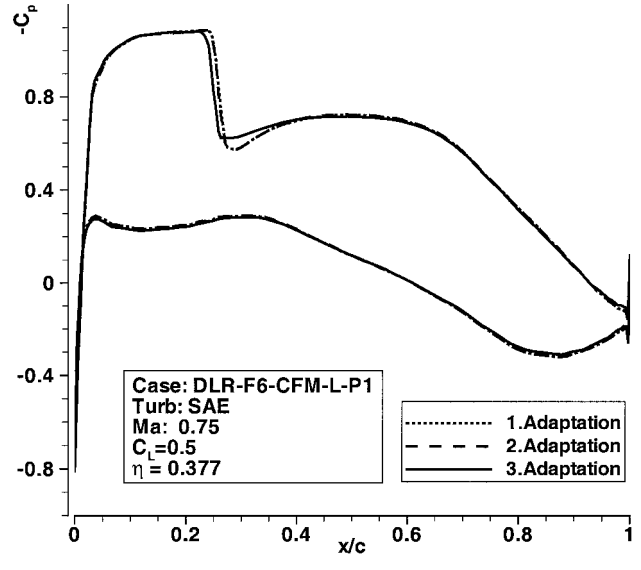

Fig. 11 Influence of grid density on pressure coefficients c_p, CFM-56-long, position 1, 37.7% half-span, $C_L = 0.5$.

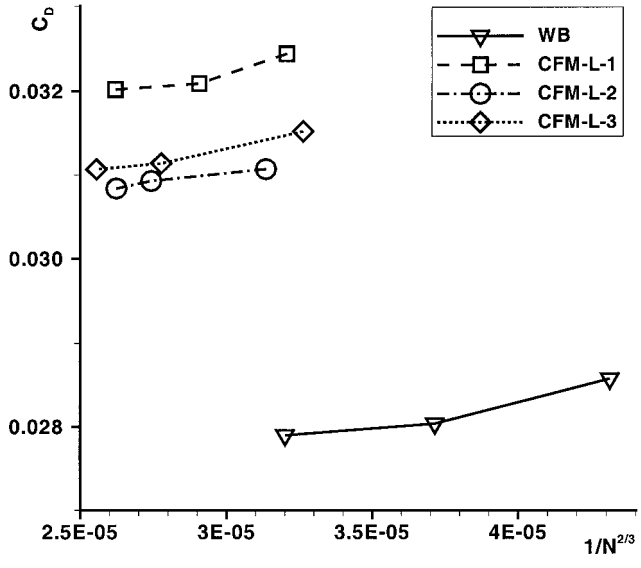

Fig. 12 Grid convergence.

Table 3 Differences of installation drag

Configurations	Drag counts, $\Delta C_{D\text{-install}}$ Experiment	Computation
CFM-long 1-CFM-long 2	10.7	11.8
CFM-long 2-CFM-long 3	3.0	2.3
VHBR-1-VHBR-2	2.0	1.7
CFM-short-VHBR-1	0.6	0.6

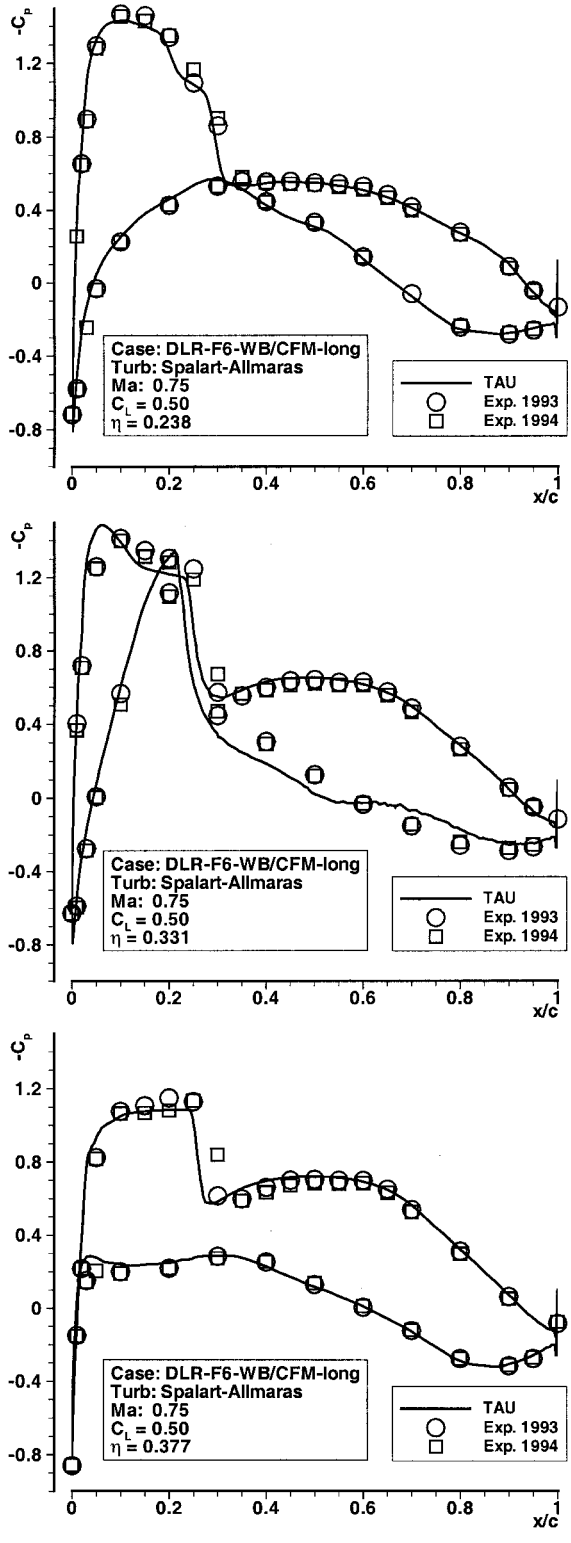

Fig. 13 Pressure coefficient c_p distributions, CFM-56-long position 1 at 23.8, 33.1, and 37.7% half-span, $C_L = 0.5$.

Grid Refinement and Grid Convergence

The influence of the grid refinement on the overall and the installation drag is visible in Fig. 10. Figure 10 shows that an increase of the number of nodes up to approximately 7.5×10^6 (approximately 24×10^6 elements) for the conventional long nacelle in areas with high flow gradients affects the installation drag in a way that the difference from the experiments is reduced. The difference between the second and third adaptation is significantly smaller than between the first and the second adaptation, although more points are inserted between the second and third step. This is an indication that a reasonable grid density has already been chosen.

The numerical solutions depend on the number of grid nodes, the order of the method, and the geometrical dimension. The solution is proportional to $1/N^{2/3}$ for a second-order accurate method in xyz space. Different strategies for the extrapolation of the solution to infinite fine grids can be found in the literature.[21,22] They are based on successively refined grids, most of structured type. Whether these strategies can be applied in a sensible way to unstructured grids is currently under discussion. An important prerequisite is that the adaptation adds points where high gradients and discretization errors occur. Otherwise, it cannot be expected that finer grids show solutions that are suited for extrapolation techniques. The adaptation

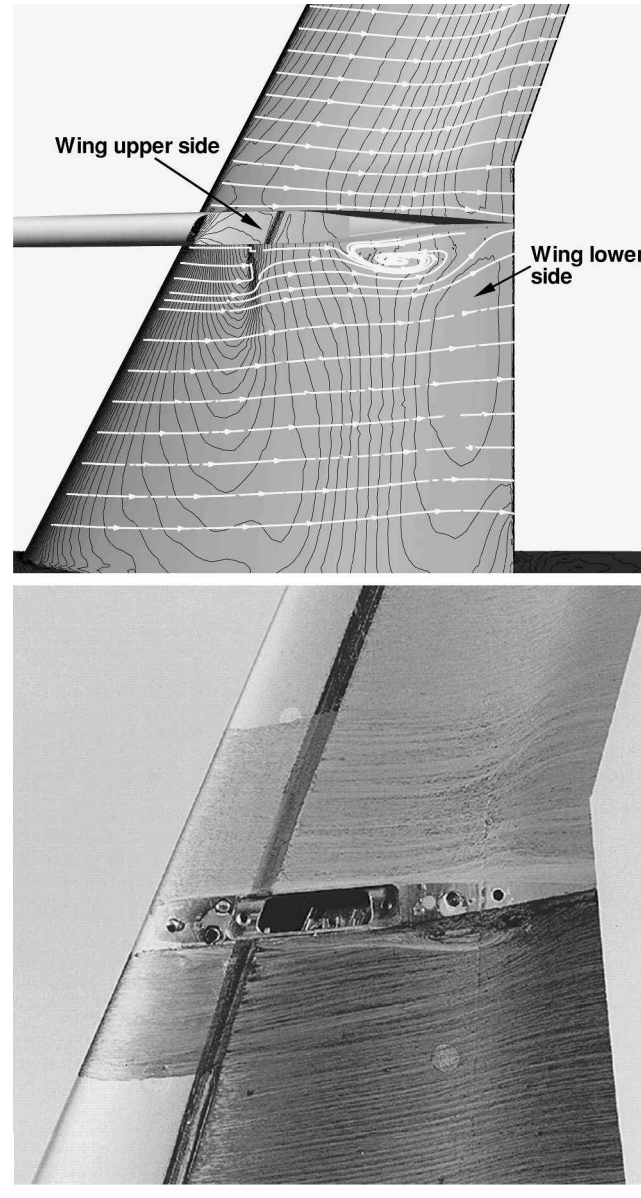

Fig. 14 Isobars and wall streamlines on lower wing CFM-56-long position 1, wind-tunnel oil-flow picture, $C_L = 0.5$.

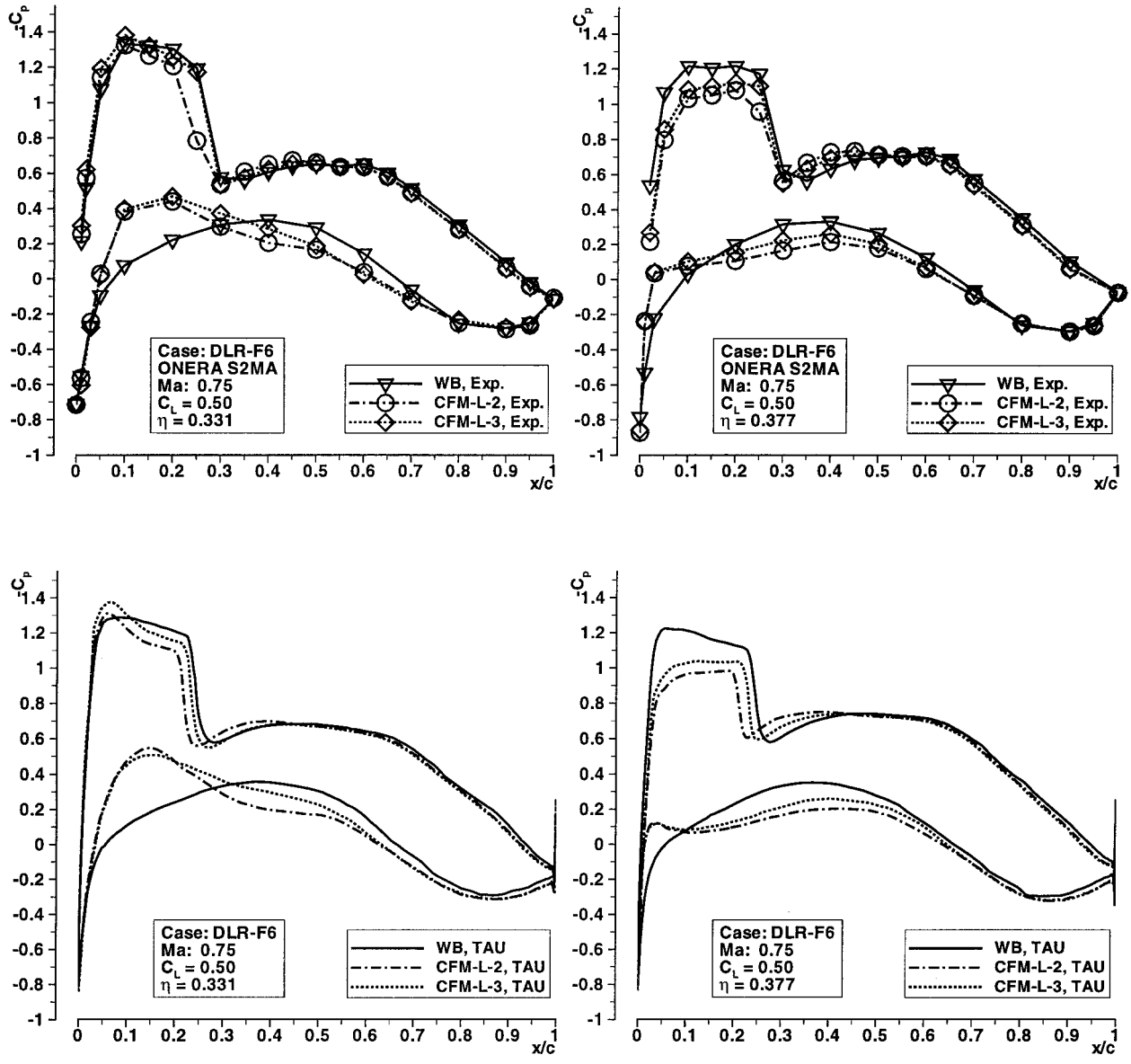

Fig. 15 Pressure coefficient c_p distributions at 33.1 and 37.7% half-span with and without CFM-56-long, positions 1, 2, 3, $C_L = 0.5$.

used in these investigations inserts points in the field and shifts the prismatic cells in the boundary layer, but it cannot insert new prismatic cells. Thus, it can be supposed that the adaptations affect the pressure slightly more than the viscous drag contributions.

Figure 11 demonstrates the influence of the grid refinement on the pressure distributions for the pylon outboard section for the conventional long nacelle at position 1. The initial grid provides a good resolution of the flow features, and only small improvements can be achieved using finer grids.

Figure 12 presents the drag vs the number of nodes for the three CFM-56-long nacelle positions and the wing–fuselage configuration. Because TAU is not second-order accurate at all points, the values are not found on a straight line. When a linear extrapolation strategy of drag using the two finest grids is applied, a change between 1.5 (5 drag counts) and 2.8% (8.8 drag counts) toward lower drag values can be computed.

Pressure Distributions

Figure 13 presents the computed pressure distribution of the CFM-56-long nacelle at position 1, which shows the strongest interference effects. The pressure measurements from two test campaigns are included and indicate the possible variation of the values, especially on the wing upper surface. For the pylon inboard section at $\eta = 0.331$, an overprediction of c_p compared to the experiments can be found at the wing nose on the upper side and on the lower wing surface, where an overprediction of a strong flow acceleration is also visible. The deviation in the rear part on the lower side is due to a separation in the wing–pylon junction. Figure 14 shows that the separation on the wing lower side close to the pylon is predicted larger than that visible in the oil-flow picture from the wind-tunnel experiments. It has been found for all configurations that if separation occurs on the lower side in the wing–pylon junction it is slightly overpredicted compared to the experiments. All other sections show a more acceptable result of c_p, for example, $\eta = 0.238$ and 0.377. The overprediction of the flow acceleration on the wing lower side of the pylon outboard section is obviously smaller than for the inboard section. The shock position is shifted upstream for all computations compared to the experimental data.

The aerodynamic influence of the other two CFM-56-long nacelle positions can be analyzed for the pylon inboard and outboard sections in Fig. 15. For these engine positions also, small overpredictions of the flow acceleration in the wing nose region are visible. This effect is found for all cases investigated and represents a systematic deviation that influences the drag but does not deteriorate the computed differences of the installation drag. When the results are compared, it is clear that the main effects such as shock

movement, flow acceleration, and deceleration can be computed, as already demonstrated with Euler calculations.[9] As stated in previous work,[18] the study shows that the interference effects are more sensitive to a shifting of the nacelles in the x direction than in the z direction.

CFM-56-Short and VHBR Nacelles

The verification has been extended to include also the conventional short and the VHBR nacelle. In contrast to the CFM-56-long nacelle, an additional inner nozzle and the overall diameter differentiate the geometries. The objective was to maintain the same grid parameter for the initial grid and to reduce unavoidable differences of the grids by successive adaptation steps. Nevertheless, the inital grid parameter needed some minor changes for the conventional short and the VHBR grids to maintain most similar prismatic cell layers, surface, and volume resolutions.

Figure 16 presents the results of the drag polar and the installation drag. The same kind of deviations as observed for the CFM-56-long nacelles exist, which verifies that a systematic effect emerges. The computed installation drag for the conventional short and the VHBR nacelles is based on the measured internal drag from the experiments. Because of the observed lower computed drag than experimental drag for all computations, it can be expected that also a lower internal drag for the nacelles with the inner nozzle could be calculated. That would shift the computational results of the installation drag slightly to higher values. The small differences of installation drag between the CFM-56-short and the two VHBR nacelle position can be computed. The result is summarized in Table 3.

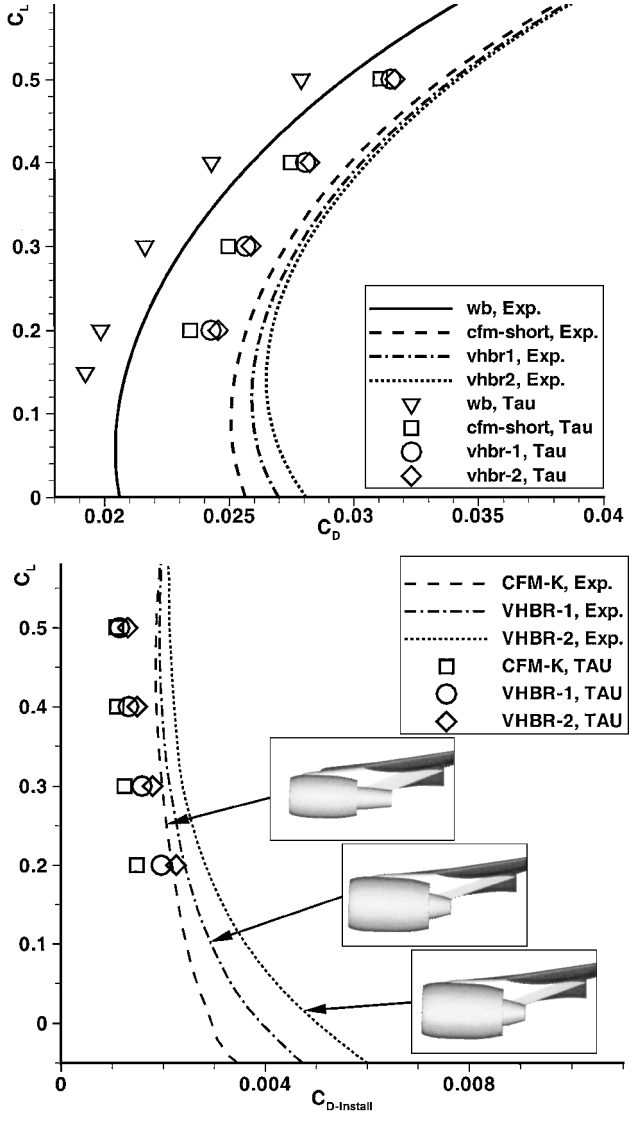

Fig. 16 Drag and installation drag coefficients for CFM-56-short and VHBR nacelles.

Conclusions

It can be concluded that an accurate computation of installation drag for engine–airframe integration design studies at cruise flight conditions applying hybrid Navier–Stokes methods is possible. The complete CFD cycle for the prediction of the installation drag for transport aircraft can be reduced to approximately one week for geometrically different configurations. When consistent and constant grid-generation and computational procedures are used, including all parameter settings, an accuracy of approximately 1% for the installation drag when compared with the experimental data can be achieved, although the total drag is predicted only with a constant offset of 6–8%. This means that differences of 1–2 drag counts of the installation drag for varying engine positions or sizes can clearly be analyzed. Grid refinement has shown that the computed installation drag values shift toward the experiments, while the total drag is reduced. This indicates that a systematic deviation of total forces between numerical and experimental results will remain, but that the differences due to the geometries can be calculated more precisely with finer grids. In a followon project, investigations will address questions of grid refinement, including the prismatic layers that had to be kept constant here, and will focus on the prediction of installation drag using hybrid techniques for powered nacelles.

References

[1]Berry, D., "The Boeing 777 Engine/Aircraft Integration Aerodynamic Design Process," *Proceedings of the 19th International Council of the Aeronautical Sciences*, Anaheim, CA, Vol. 2, 1994, pp. 1305–1319; also International Council of the Aeronautical Sciences, ICAS Paper 94-6.4.4, 1994.

[2]Hurez, A., "Recent Progress on Powerplant/Airframe Integration at Aerospatiale Matra Airbus," *Proceedings of Workshop on EU-Research on Aerodynamic Engine/Aircraft Integration for Transport Aircraft*, edited by H. Hoheisel, DLR, Braunschweig, Germany, 2000, pp. 2.1–2.10.

[3]Burgsmüller, W., Hoheisel, H., and Kooi, W., "Engine/Airframe Interference on Transport Aircraft with Ducted Propfans—The European Research Program DUPRIN," International Council of the Aeronautical Sciences, ICAS Paper 94-3.7.1, 1994.

[4]Burgsmüller, W., Rollin, C., and Rossow, C.-C., "Engine Integration on Future Transport Aircraft—The European Research Program DUPRIN/ENIFAIR," International Council of the Aeronautical Sciences, ICAS Paper 98-5.6.2, 1998.

[5]Rudnik, R., and Rossow, C.-C., "Numerical Simulation of Engine/Airframe Integration for High-Bypass Engines," ECCOMAS-2000 Paper [CD-ROM], Barcelona, Spain, 2000.

[6]Laban, M., "Aircraft Drag and Thrust Analysis, Project Overview and Key Results," *Proceedings of Workshop on EU-Research on Aerodynamic Engine/Aircraft Integration for Transport Aircraft*, edited by H. Hoheisel, DLR, Braunschweig, Germany, 2000, pp. 9.1–9.15.

[7]von Geyr, H. F., "Key Results of Detailed Thrust and Drag Studies on the ALVAST Configuration," *Proceedings of Workshop on EU-Research on Aerodynamic Engine/Aircraft Integration for Transport Aircraft*, edited by H. Hoheisel, DLR, Braunschweig, Germany, 2000, pp. 12.1–12.17.

[8]von Geyr, H. F., Brodersen, O., and Melber, S., "Engine Integration on Transport Aircraft—The European Research Activities on Propulsion Airframe Integration," ECCOMAS-2001 Paper [CD-ROM], Swansea, UK, 2001.

[9]Rossow, C.-C., Godard, J.-L., Hoheisel, H., and Schmitt, V., "Investigation of Propulsion Integration Interference on a Transport Aircraft Configuration," AIAA Paper 92-3097, July 1992.

[10]Rill, S., and Becker, K., "Simulation of Transonic Flow over Twin-Jet Transport Aircraft," *Journal of Aircraft*, Vol. 29, No. 4, 1992, pp. 640–646.

[11]Kao, T., Su, T., and Yu, N., "Navier–Stokes Calculations for Transport Wing–Body Configurations with Nacelles and Struts," AIAA Paper 93-2945, July 1993.

[12]Greff, E., Becker, K., Karwin, M., and Rill, S., "Integration of High Bypass Ratio Engines on Modern Transonic Wings for Regional Aircraft," *Aeronautical Journal of the Royal Aeronautical Society*, Jan. 1993, pp. 1–13.

[13]Rossow, C.-C., and Hoheisel, H., "Numerical Study of Interference Effects of Wing-Mounted Advanced Engine Concepts," International Council of the Aeronautical Sciences, ICAS Paper 94-6.4.1, 1994.

[14]Chaput, E., Gacherieu, C., and Tourette, L., "Application of Navier–Stokes Methods for Engine/Airframe Integration," *Proceedings of DLR*

Workshop on Aspects of Engine–Airframe Integration for Transport Aircraft, edited by H. Hoheisel, German Aerospace Research Center, DLR, TR 96-01, Brunswick, Germany, 1996, pp. 7.1–7.12.

[15]Hoheisel, H., "Aerodynamic Aspects of Engine-Aircraft Integration of Transport Aircraft," *Aerospace Science and Technology*, No. 7, 1997, pp. 475–487.

[16]Godard, J.-L., Hoheisel, H., Rossow, C.-C., and Schmitt, V., "Investigation of Interference Effects for Different Engine Positions on a Transport Aircraft Configuration," *Proceedings of DLR Workshop on Aspects of Engine-Airframe Integration for Transport Aircraft*, edited by H. Hoheisel, German Aerospace Research Center, DLR, TR 96-01, Brunswick, Germany, 1996, pp. 11.1–11.22.

[17]Rossow, C.-C., "Efficient Computations of Inviscid Flow Fields Around Complex Configurations Using a Multiblock Multigrid Method," *Applied Numerical Methods*, Vol. 8, 1992, pp. 735–747.

[18]Godard, J.-L., Hoheisel, H., Rossow, C.-C., and Schmitt, V., "Investigation of Interference Effects for Different Engine Positions on a Transport Aircraft Configuration," *Proceedings of DLR Workshop on Aspects of Engine-Airframe Integration for Transport Aircraft*, edited by H. Hoheisel, German Aerospace Research Center, DLR, TR 96-01, Brunswick, Germany, 1996, pp. 11.1–11.22.

[19]Godard, J.-L., Brodersen, O., and Hepperle, M., "Aerodynamic Interference Effects with Engines of Different Bypass Ratio on the Generic F6 Transport Aircraft Configuration," *Proceedings of the 7th European Propulsion Forum: Aspects on Engine/Airframe Integration*, Confederation of European Aerospace Societies, 1999, pp. 75–84.

[20]Brodersen, O., and Rossow, C.-C., "Calculation of Interference Phenomena for a Transport Aircraft Configuration Considering Viscous Effects," *Proceedings of European Forum: Recent Developments and Applications in Aeronautical CFD*, Royal Aeronautical Society, 1993, pp. 6.1–6.1.

[21]Roache, P., "Verification of Codes and Calculations," *AIAA Journal*, Vol. 36, No. 5, 1998, pp. 696–702.

[22]Oskam, B., and Sloof, J., "Recent Advances in Computational Aerodynamics at NLR," AIAA Paper 98-0138, June 1998.

[23]Habashi, W., Dompierre, J., Bourgault, Y., Fortin, M., and Vallet, M.-G., "Certifiable Computational Fluid Dynamics Through Mesh Oprimization," *AIAA Journal*, Vol. 36, No. 5, 1998, pp. 703–711.

[24]Jameson, A., and Martinelli, L., "Mesh Refinement and Modelling Errors in Flow Simulation," *AIAA Journal*, Vol. 36, No. 5, 1998, pp. 676–685.

[25]Kroll, N., Rossow, C.-C., Becker, K., and Thiele, F., "MEGAFLOW—A Numerical Flow Simulation System," International Council of the Aeronautical Sciences, ICAS Paper 98-2.7.4, 1998.

[26]Brodersen, O., Monsen, E., Ronzheimer, A., Rudnik, R., and Rossow, C.-C., "Computations of Aerodynamic Coefficients for the DLR-F6 Configuration Using MEGAFLOW," *Notes on Numerical Fluid Mechanics*, edited by W. Nitsche, H.-J. Heinemann, and R. Hilbig, Vol. 72, Vieweg, Brunswick, Germany, 1998, pp. 85–92.

[27]Jameson, A., Baker, T., and Weatherill, N., "Calculation of Inviscid Transonic Flow over a Complete Aircraft," AIAA Paper 86-0103, Nov. 1986.

[28]Venkatakrishnan, V., "Perspective on Unstructured Grid Flow Solvers," *AIAA Journal*, Vol. 34, No. 3, 1996, pp. 533–547.

[29]Mavriplis, D., "Parallel Performance Investigations of an Unstructured Mesh Navier–Stokes Solver," International Council of the Aeronautical Sciences, ICAS Rept. 2000-13, 2000; also NASA CR-2000-21088, 2000.

[30]Gerhold, T., Galle, M., Friedrich, O., and Evans, J., "Calculation of Complex Three-Dimensional Configurations Employing the DLR-TAU Code," AIAA Paper 97-0167, March 1997.

[31]Galle, M., "Ein Verfahren zur numerischen Simulation kompressibler, reibungsbehafteter Strömungen auf hybriden Netzen," German Aerospace Research Center, DLR, TR FB-99-04, Brunswick, Germany, 1999.

[32]Gerhold, T., Evans, J., "Efficient Computation of 3D-Flows for Complex Configurations with the DLR-TAU Code Using Automatic Adaptation," *Notes on Numerical Fluid Mechanics*, edited by W. Nitsche, H.-J. Heinemann, and R. Hilbig, Vol. 72, Vieweg, Brunswick, Germany, 1998, pp. 178–185.

[33]Schwamborn, D., Gerhold, T., and Hannemann, V., "On the Validation of the DLR-TAU Code," *Notes on Numerical Fluid Mechanics*, edited by W. Nitsche, H.-J. Heinemann, and R. Hilbig, Vol. 72, Vieweg, Brunswick, Germany, 1998, pp. 426–433.

[34]Kallinderis, Y., "Hybrid Grids and Their Applications," *Handbook of Grid Generation*, edited by J. F. Thompson, B. K. Soni, and N. Weatherill, CRC Press, Boca Raton, FL, 1999, pp. 25.1–25.18.

[35]Khawaja, A., and Kallinderis, Y., "Hybrid Grid Generation for Turbomachinery and Aerospace Applications," *International Journal for Numerical Methods in Engineering*, No. 49, 2000, pp. 145–166.

[36]Rudnik, R., Melber, S., Ronzheimer, A., and Brodersen, O., "Three-Dimensional Navier–Stokes Simulations for Transport Aircraft High-Lift Configurations," *Journal of Aircraft*, Vol. 38, No. 5, 2001, pp. 895–903.

[37]Redeker, G., "DLR-F4 Wing Body Configuration," AGARD Rept. AR-303, 1994, pp. 4.1–4.21.

[38]Spalart, P., and Allmaras, S., "A One-Equation Turbulence Model for Aerodynamic-Flows," AIAA Paper 92-0439, Aug. 1992.